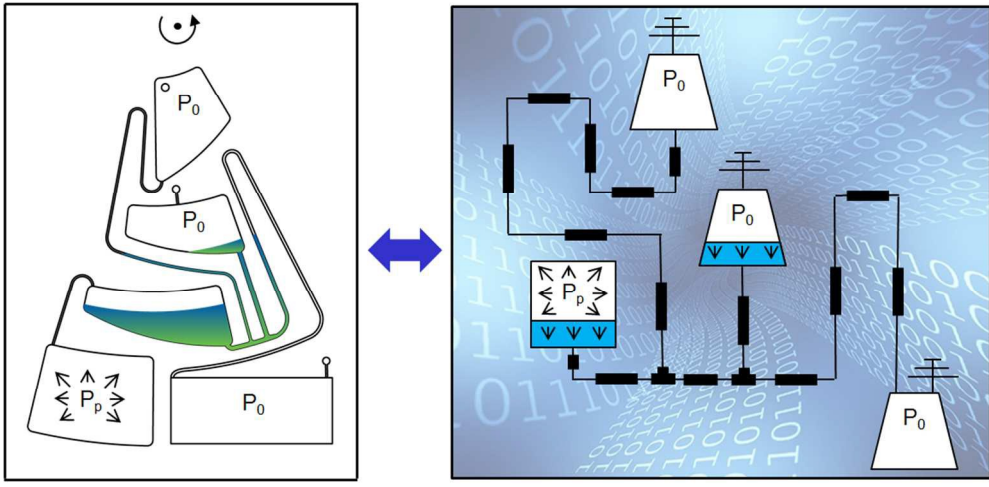# Lab on a Chip

Accepted Manuscript

This is an *Accepted Manuscript*, which has been through the Royal Society of Chemistry peer review process and has been accepted for publication.

Accepted Manuscripts are published online shortly after acceptance, before technical editing, formatting and proof reading. Using this free service, authors can make their results available to the community, in citable form, before we publish the edited article. We will replace this *Accepted Manuscript* with the edited and formatted *Advance Article* as soon as it is available.

You can find more information about *Accepted Manuscripts* in the **Information for Authors**.

ROYAL SOCIETY OF CHEMISTRY

www.rsc.org/loc

Journal Name

ARTICLE

System-level network simulation for robust centrifugal-microfluidic lab-on-a-chip systems

I. Schwarz[a], S. Zehnle[a], T. Hutzenlaub[a,b], R. Zengerle[a,b,c], N. Paust[a,b]

Centrifugal microfluidics shows a clear trend towards a higher degree of integration and parallelization[1]. This trend leads to an increase in number and density of integrated microfluidic unit operations. The fact that all unit operations are processed by the same common spin protocol turns higher integration into higher complexity. To allow for efficient development anyhow, we introduce advanced lumped models for network simulations in centrifugal microfluidics. These models consider the interplay of centrifugal and Euler pressures, viscous dissipation, capillary pressures and pneumatic pressures. The simulations are fast and simple to set up and allow for the precise prediction of flow rates as well as switching and valving events. During development, channel and chamber geometry variations due to manufacturing tolerances can be taken into account as well as pipetting errors, variations of contact angles, compliant chamber walls and temperature variations in the processing device. As an example for considering these parameters during development, we demonstrate simulation based robustness analysis for pneumatic siphon valving in centrifugal microfluidics.

Subsequently the influence of liquid properties on pumping and valving is studied for four liquids relevant for biochemical analysis, namely: water (large surface tension), blood plasma (large contact angle hysteresis), ethanol/water (highly wetting) and glycerine/water (highly viscous). In a second example, we derive a spin protocol to attain a constant flow rate under varying pressure conditions. Both examples show excellent agreement to experimental validations.

Introduction

Centrifugal microfluidics has evolved to one of the most promising technologies for miniaturization, automation and parallelization of laboratory workflows especially for Point-of-Care applications. A large set of unit operations covering the entire range of liquid handling from sample and reagent supply to readout is available. Among the recently published papers, a clear trend towards sample to answer systems on centrifugal microfluidic lab-on-a-chip platforms is obvious. This trend has led to the integration of a constantly increasing number of assay steps into a single disc[1-3].

However, all unit operations on a centrifugal disc need to operate under the influence of one common spin protocol. This turns higher integration into higher complexity[4,5]. One way to tackle this challenge is the use of active valves (controlled by external means such as heat sources) to decouple the valving event from the spin protocol. A prominent example is the integration of wax valves for liquid control that are actuated via

a laser diode to open a normally closed or close a normally open valve[6]. Similarly, laser radiation has been applied to selectively open connections between microfluidic chambers by melting of the polymer disk material at predetermined points[7].

In another approach, the ambient is heated up in order to increase the air pressure in fluidic chambers so that the containing liquid is displaced through a siphon before it is drained off[8]. Aeinehvand et. al. introduced reversible thermopneumatic valves, based on the deflection of a latex membrane to open or close the valve[9].

In contrast to such actively controlled valves, passive valves are controlled by the rotational protocol, only, and omit the use of external components, such as lasers or heaters. Amongst these are normally closed capillary valves that open in case that the centrifugal pressure of a liquid column exerts the capillary back pressure at geometric edges or hydrophobic patches[10,11]. Vice versa, capillary siphon valves open at low rotational speed when the capillary pressure prevails over the centrifugal pressure and lifts the liquid over the siphon crest[5,12].

The number of valving parameters can be increased by the introduction of ancillary materials into the platform. R. Gorkin III et al. developed dissolvable film valves that allow for air entrapment between a liquid column and the dissolvable film in normally closed state at low spin speed. Inversion of the liquid and gas phases at high spin speed opens the valves irreversibly[13]. This principle has been fleshed out using multiple dissolvable films to realize event-triggered and timed valving by specifically venting pneumatic chambers[14] .

While capillary valves highly depend on channel geometries and wetting properties, methods using auxiliary materials entail additional manufacturing steps for adding wax, dissolvable films or flexible latex membranes, which increase cost in mass fabrication and increases complexity of the device in case of irradiation heat controlled valving techniques. Further concerns may be the robustness of dissolvable films or the compatibility of additional wax with biochemical analysis. To avoid possible contaminations through contact of wax with the processed liquid, fluid control by opening and closing air vents with wax valves is of advantage[15].

Alternatively, monolithically integrated structures have been presented that use on disc generated pneumatic pressure for valving, switching and pumping[16,17–19]. The introduction of pneumatic pumping for example[18–21] has enabled the implementation of substantially longer assay reaction sequences by repeated use of the radial distance on the disc. Due to the high pneumatic pressures used, pneumatic fluid control is widely independent of liquid properties and contact angles and therefore allows for robust liquid processing without auxiliary means. However, pneumatic fluid control is based on a complex interplay of different rapidly changing forces such as centrifugal and pneumatic pressures as well as pressure loss by viscous dissipation. Thus, design tools are required to correctly describe the dynamic behaviour, in particular in the context of a high number of integrated fluidic unit operations controlled by the same spin protocol.

For practical reasons, these design tools need to allow for a simple and fast description of the system and a subsequent fast calculation of the system dynamics. One way to approach this need is to use a set of directly solvable analytical equations. This requires to restrict the used structure geometries of the unit operations to simplified geometries and quasi static operation conditions that are amenable to analytical description[2,18,20,22]. The second approach is to use numerical simulation to describe the interplay of different centrifugal microfluidic unit operations. In this paper we advocate the latter approach due to its potential to greatly improve understanding of complex systems, reduce development time and to provide robustness analysis under varying operation conditions.

In order to correctly describe fluid handling in centrifugal microfluidic lab-on-a-chip systems, fluid flow rates in channels, as well as valving and switching events need to be described

correctly by a suitable simulation tool. To this end, the prediction of the propagation of liquid/gas interfaces is essential. Simulation techniques using fine grained discretization[23] can be ruled out for standard layout tasks as they lead to prohibitively high computational costs for the simulation of moving two-phase interfaces[24].

A suitable alternative are system-level network-simulations, based on easily combinable coarse grained element models – analogous to the well-known tools used for simulation of electrical networks. First works in the area of general fluidic networks were contributed by Schaedel et.al.[25] An overview of this approach for the design of pressure driven microfluidic networks is given by Oh et. al.[26]. In the area of pressure-driven droplet microfluidics Schindler et. al.[27] and Jousse et. al.[28] contributed lumped models and Gleichmann et. al. developed a toolkit for network-simulation[29]. Koltay et al. used lumped models for the simulation of free jet ejection in printing applications[30]. Lumped models for capillary self-priming in microfluidic channel networks were contributed by Sesterhenn et al[31]. Based on this work, Zehnle et al[21] first used lumped models to simulate centrifugo-dynamic pumping in centrifugal microfluidics. In the present work, we explain the model implementation in detail and introduce new advanced lumped models and simulation strategies that account for capillary forces and contact angle hysteresis, water vapour pressure, material compliance and manufacturing tolerances. In addition, a method for simulation based flow rate control is discussed.

Network simulation principle

In system-level network-simulation, a network of distinct physical elements is represented by a network of model blocks with identical topology. In analogy to modelling integrated circuits in electronics through a network of model blocks which represent e.g. electrical conductors, capacitors and inductors, a centrifugal microfluidic network is modelled by model blocks which represent channels, chambers etc.
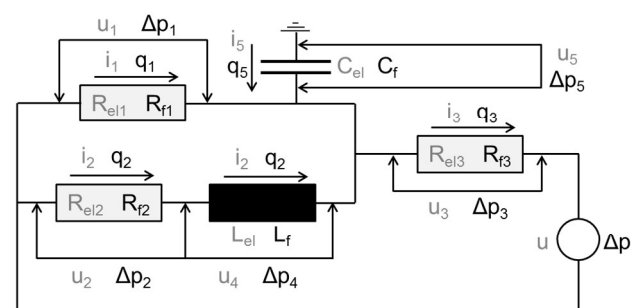
u, i, R_{el}, C_{el}, L_{el}: Electrical quantities | Δp, i, R_f, C_f, L_f: Corresponding fluidic quantities

Figure 1: Analogy between electrical and fluidic networks for the example of a flow divider including capacities and inductivities. Electric variables and parameters are depicted in grey, fluidic variables and parameters in black The across variables voltage source (u) or voltage drops ($u_{1,2,3}$) in electrical engineering correspond to pressure source (Δp) and pressure drops ($\Delta p_{1,2,3}$). The through variable current (i) corresponds to the volumetric flow rate (q). Model parameters such as the electric resistance ($R_{el1,2,3}$) capacitance (C_{el}) or inductance

(L_{el}) correspond to the fluidic resistance ($R_{f1,2,3}$) capacitance (C_f) and inertia (L_f), respectively. Pressure drops typically originate from fluidic resistance, capacitance and inertia. Pressure sources can have multiple origins. In centrifugal microfluidics, pressure sources can be Centrifugal, Euler, inertial, pneumatic, or capillary pressures.

In general, a lumped model of an element describes the relation between the across- and through-variable of said element. This relation is simulated with transfer functions for which model parameters such as the fluidic resistance, capacitance or inertia are derived from model geometry and operation conditions. The analogies between electronic and fluidic networks for across- and through variables as well as for some model parameters are illustrated in Fig. 1. The across-variable thereby stands for the driving force for a conserved flow and the through-variable for said conserved flow. In this work, we chose the pressure-difference Δp between inlet port and outlet port of a model block as across-variable and the corresponding volume flow q as through-variable as schematically depicted in Figure 2. The operation conditions of an element comprise all factors that influence its behaviour, i.e. its wetting state (full, empty, partially filled, etc.), the spin and temperature protocols and the liquid properties.

All elements of the network model – the model blocks – need to be provided with their individual values for geometry, position, contact angle etc. in the considered network. Global parameters common to all model blocks are used to specify the liquid properties (i.e. dynamic viscosity η, liquid density ρ, surface tension σ). The time dependent spin and temperature protocols are provided to the model blocks via signal blocks. These signal blocks transmit the pre-defined protocols to the respective input ports of the model blocks. To account for the dependency of the relationship between Δp and q on operation conditions, such as liquid volume inside a channel or the amount of gas inside an unvented chamber, block internal variables are used.
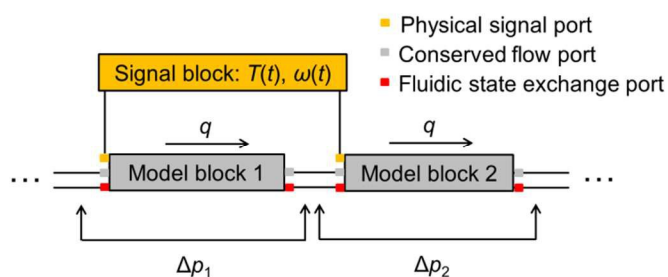

Figure 2: Schematic example for the representation of centrifugal microfluidic networks through networks of lumped model blocks. Model block 1 and model block 2 represent two connected channels with different geometries and contact angles. Δp is the across variable and q the through-variable. Both channels are provided with the temperature and spin protocol through their "physical signal ports". The conserved flow is exchanged between the model blocks through the "conserved flow ports". In addition to the flow from one block to the next, the blocks exchange information about their fluidic states – i.e. whether they are completely filled, empty or partially filled – through "fluidic state ports". During simulation, the solver ensures Kirchhoffs laws for the conserved flow q and the corresponding pressure differences Δp for all connected model blocks.

Crucial for the network simulation of two phase fluidics is the propagation of the wetting state information from one model block to the next – i.e. whether a channel is full of liquid, partially filled, or empty. A procedure for this communication has been described by Sesterhenn et al.[31] for the Saber simulation environment and purely capillary channel-networks. Adapted to the Simscape programming language, this communication procedure is also used for the implementation of the lumped models in the present work as further detailed in the paragraph "wetting states and phase information propagation" and sections S3 & S4 of the electronic supplement.

All model blocks that represent the fluidic network are put together by pick and place. Subsequently, a compiler automatically generates a system of differential-algebraic equations (DAE) from the network of parameterized lumped models. To solve the DAE system, settings such as the solver to be used and the time to simulate need to be specified. Commercially available solvers are used to rapidly solve the DAE system in a robust manner. The result of the simulation is the full information about the values of Δp and q for all model-blocks as well as the values of all model block internal variables during system operation. These comprise e.g. liquid volumes and amounts of gas in chambers as well as the individual pressure contributions of e.g. vapour pressure, centrifugal pressure, inertial pressure, capillary pressure and Euler pressure. In this work, the Simscape simulation package of MathWorks Inc., USA has been used in the version R2015a.

In Figure 3, the fluidic structure discussed in this paper is depicted together with its model block representation. The example considers the supply of liquid in the *inlet chamber*, subsequent mixing by reciprocation between *pneumatic chamber 1* and *mixing chamber* through the *mixing channel* – as previously introduced by Norozi et al.[32] – and finally pneumatic siphon valving[17] into a downstream fluidics. Details of the fluidics are discussed later in application case 1.

Each of the fluidic elements – such as channels, chambers or T-junctions – is represented by a corresponding model block. The implementation of the considered physical effects in the model blocks is explained in detail in the following section. The physical effects of centrifugal microfluidics in general have been discussed extensively in the literature [1,3,33].
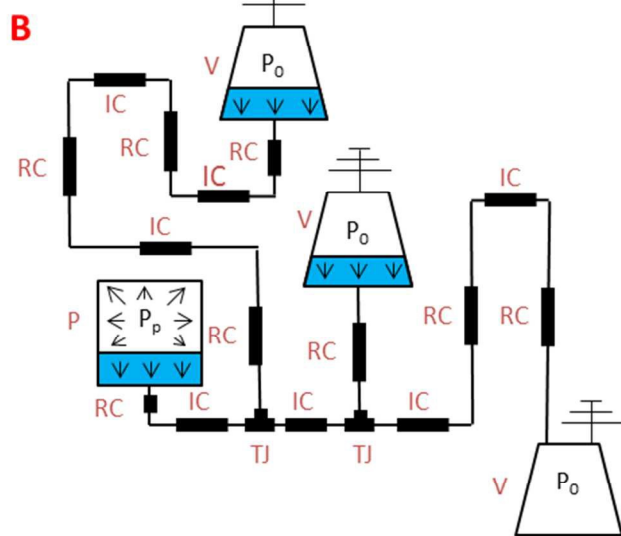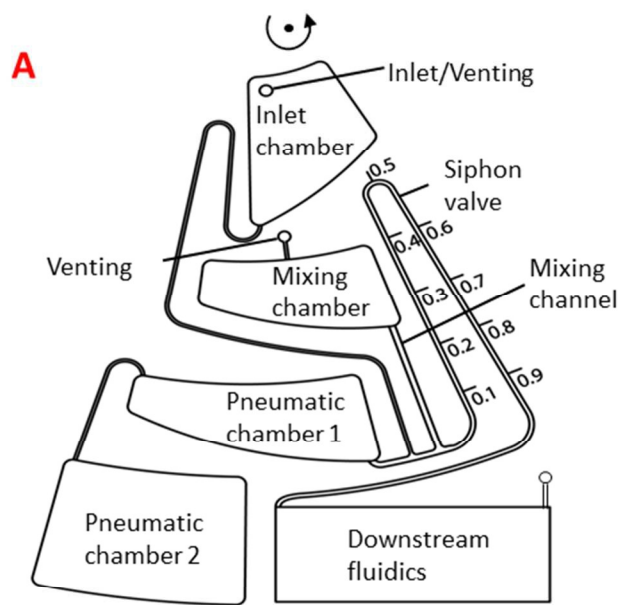
Models in centrifugal microfluidics

Channel models

Most channel networks with arbitrary orientations can be approximated by a network of two types of channels: radially oriented channels and iso-radially oriented channels. In contrast to models for channels with arbitrary orientation, channel models with fixed orientations are more straight-forward to use. We will demonstrate, that they are sufficient for accurate simulation predictions under the conditions of the exemplary application cases. Furthermore, we describe a procedure for

modelling channels with arbitrary orientation via an equivalent network of radial and isoradial channels in section S1.1 of the electronic supplement. A schematic of the channel models is depicted in Figure 4. In cases, where the proposed idealization of centrifugal microfluidic channel networks by radial and isoradial channels is insufficient, it is also possible to directly simulate curved channels. A corresponding procedure is discussed in section S1.2 of the electronic supplement.

B) Model block representation of the fluidic network. The model consists of blocks for "radial" and "isoradial" channels, channel junctions, vented chambers and pneumatic chambers (unvented). A connection to ambient pressure is indicated by the ground symbol.

RADIAL CHANNELS are channels with an orientation along the radius of the centrifugal disc. In these channels, pressure differences between inlet and outlet due to viscous dissipation of liquid and gas are considered as well as centrifugal, inertial and capillary pressures. Table 1 lists the corresponding expressions for the different pressure terms. The used formula for the fluidic resistance of a rectangular channel deviates from the analytical result by less than $1.14 * 10^{-4}$ % for all aspect ratios $\frac{d}{w} \leq 1$ and provides thereby good accuracy at low computational cost. The derivation of the error estimation is given in section S9 of the electronic supplement. For radial channels, the Euler pressure is neglected as it is always oriented towards the channel walls and does not contribute to the overall fluidic behaviour.

Figure 3: A) 2D sketch of the fluidic structure used in this work to demonstrate the potential of the network simulation approach for centrifugal microfluidics. Due to space limitations of the overall fluidics, the gas volume of the pneumatic chamber was divided between the pneumatic chambers 1 & 2. The scale on the siphon indicates the fill level of the siphon during valving.

Table 1: Considered physical effects in channel models. ρ denotes the density of the considered liquid. r stands for the radial distance from the centre of rotation to the most distant point of a radial or isoradial channel. ω denotes the angular spin frequency of the considered disc. The liquid filled length inside a channel is given by l. The projections of l on the radial and isoradial directions are given by l_r and l_i. For an isoradial channel $l_i = l$ and $l_r = 0$ hold, for a radial channel l_r and l_i are exchanged. The flow rate through a channel is q. The width and depth of a rectangular channel are specified by w and d, respectively. The fluidic resistance R_f depends on the shape of the cross-section of the channel as indicated by C_g. For the liquids, the dynamic viscosity, surface-tension and contact angle with the substrate are specified by η, σ and θ.

Centrifugal pressure[21]	$p_{cent} = \frac{\rho}{2} \omega^2 (r^2 - (r - l_r)^2)$
Euler pressure[21]	$p_{euler} = \rho\, l_i \frac{d\omega}{dt}\, r$
Inertial pressures[21]	$p_{inert} = \frac{\rho\, l}{w\, d} \frac{dq}{dt}$
Viscous dissipation[33]	$p_{visc} = R_f\, q$, with $R_f = C_g \frac{\eta\, l}{A^2}$ Square cross section: $C_g = 28.4$ Rectangular cross section: $C_g = \dfrac{12}{\frac{d}{w}\left(1 - \frac{192\, d}{\pi^5\, w}\left(\tanh\frac{\pi\, w}{2\, d} + \frac{31}{32}\zeta(5) - 1\right)\right)}$ Geometry factors for trapezoidal and other cross-sections can be found in [33,34]
Capillary pressures[33]	$p_{cap} = \sigma\left(\frac{\cos(\theta_1) + \cos(\theta_2)}{w} + \frac{\cos(\theta_3) + \cos(\theta_4)}{d}\right)$

V: Volume chamber   P: Pneumatic chamber
IC: Isoradial channel   RC: Radial channel   TJ: T-Junction

In channels, the Coriolis force leads to a deformation of the flow pattern[35], which can be used for mixing[36] of liquids and results in a complex nonlinear dependency of the fluidic resistance on the flow-rate, the channel geometry and the angular velocity of the moving disc. In order to quantify the impact of this complex flow pattern dependent effect on the fluidic behaviour of the studied fluidic network, we performed 3D-CFD-simulations of the effect with COMSOL Multiphysics® 5.1 (www.comsol.com, 2015). The simulations show that the effect can be neglected for the discussed application cases. For this reason, the effect was also neglected in the performed network-simulations. Details are provided in section S 7 of the electronic supplement. If required, Coriolis forces could be considered for the fluidic resistance via fit functions derived from 3D-CFD-simulations. Main influence parameters are spin frequency, flow rate, and the cross-section of the channel.

The transfer functions of lumped models depend on their wetting state. For viscous dissipation, centrifugal and inertial pressures, this dependency is given by the liquid filled length l of the channel and its radial and isoradial components l_r and l_i as indicated in Table 1. For capillary pressures, four discrete cases need to be considered. In completely filled and empty channels, capillary pressure does not contribute. In partially filled channels, the contribution of capillary pressure has a positive or a negative sign, dependent on the direction of filling (see Figure 4). The transfer function of a radial channel can be written as:

$$\Delta p + p_{cent} + C * p_{cap} = p_{inert} + p_{visc} \quad (1)$$

where C indicates the different wetting cases and is 0 for full and empty channels and +1 / -1 for a channel filled partially from the radially inward or radial outward side, respectively.
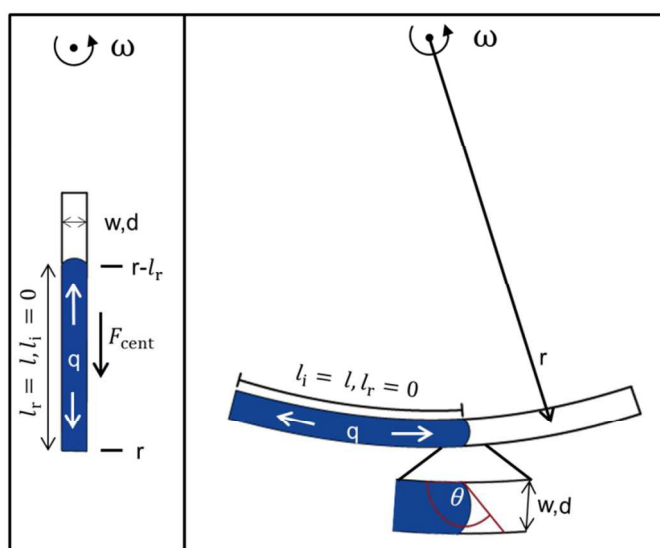
In order to track the liquid meniscus position, each channel has an internal variable V for the liquid volume inside the channel which changes dependent on the wetting state. For an empty or full channel, $\dot{V}$ is zero whereas for a partially filled channel, $\dot{V} = \pm q$ holds, dependent on the direction of filling.

ISORADIAL CHANNELS are channels with a constant distance from the centre of rotation. These channels are modelled analogously to radial channels with two differences: They consider Euler pressures and omit centrifugal pressures. The corresponding expressions are listed in Table 1.

SPECIALIZED CHANNEL MODELS, that only need to account for a subset of the effects considered by regular channel models – such as for example through holes in multilayer fluidics, which only consider viscous dissipation, inertial and capillary pressure – can be generated simply by deleting the not relevant terms in radial or isoradial channel models.

WETTING STATES AND PHASE INFORMATION PROPAGATION In order to propagate phase information from one model block to the next, wetting state signals are exchanged between adjacent blocks. These signals reflect whether the respective connection is currently wet (1) or dry (0) and determine the wetting state of a model block. Changes in the wetting state of model blocks are triggered either if the wetting state signal coming from a connected block changes, or if the internal variable V indicates that the channel has been filled or emptied completely. An exemplary scenario explaining the exchange of phase information is depicted in Figure 5. All transfer functions, the equations for the internal variables, and the wetting state signals sent to the connected model blocks depend on the wetting state of the model block. The implementation of this dependency is done via a conditional selection of the correct set of equations based on the incoming wetting state signals and additional information such as the current direction of flow, as further detailed in the following subsection and sections S2-S4 in the electronic supplement.
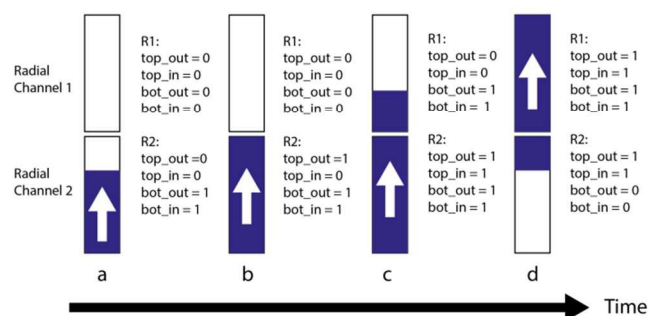

Figure 4: Illustration of channel models. All geometry related variables are identical to Table 1. **Left:** Illustration of a radially oriented partially filled channel. The radial position of the channel on the disc is defined by the largest distance between centre of rotation and radial channel r. **Right:** Illustration of an isoradially oriented, partially filled channel. Here r determines the radial position of the isoradial channel.

Figure 5: Schematic of the wetting state information propagation from one radial channel to the next. The wetting-state communication is performed through the wetting state signals top_in, top_out, bot_in and bot_out indicated in the Figure. The signals from the output port of one channel are connected to the input port of the next channel. In this example, the liquid flow is directed radially inwards.

From left to right: a) Radial channel 2 is partially filled with liquid from the bottom (radially outward port). This is indicated by the value 1 (for wet) for the two bottom signals of radial channel 2 and the value 0 (for dry) for the two top signals.

b) Radial channel 2 has run full. This event leads to a change of the internal fluidic state of radial channel 2 i.e. the wetting state signal top_out changes from dry to wet. The top_out signal is propagated to the bot_in signal port of radial channel 1. Upon change of bot_in in radial channel 1 from dry to wet, it changes its wetting state and therefore changes its signal bot_out from dry to wet.

c) shows the wetting states of the two channels after this information exchange. Radial channel 2 is completely filled and channel 1 is partially filled from the bottom.

d) Radial channel 1 is completely filled and radial channel 2 is in the process of being emptied to the top.

CAPILLARY PRESSURES are calculated in channel models based on the equation described in Table 1. In order to account for capillary hysteresis, i.e. the dependency of capillary pressure on the direction of flow, channel models can be provided with an advancing and a receding contact angle. If the direction of liquid flow changes during simulation, the contact angle does not change abruptly from advancing to receding or vice versa. Instead, capillary pressures are interpolated between the advancing and receding value. This is achieved through the variable V_{cap} which represents a virtual Volume to describe how far a change from the advancing to the receding contact angle or vice versa has been proceeded after a change of flow direction. V_{cap} is calculated by integrating the liquid flow. The parameter $V_{cap\ max}$ bounds this integration. I.e. the liquid flow integration by V_{cap} is stopped if the value of V_{cap} exceeds the interval $[-V_{cap\ max}, V_{cap\ max}]$. Therefore, the expression $V_{cap}/V_{cap\ max}$ can be used for linear interpolation between the capillary pressures. The consideration of contact angle hysteresis allows to correctly describe the liquid behaviour in cases where capillary pressures are dominant. An important case is when the advancing contact *angle between liquid and substrate is > 90° and the receding contact* angle < 90°. Here the approximation with only one contact angle ($\neq$ 90°) would lead to a wetting or de-wetting behaviour, whereas the consideration of capillary hysteresis leads to a stop of liquid meniscus movement in absence of other pressures. Details of the implementation of capillary pressure calculation as well as the procedure for handling coating liquids – such as blood plasma – are provided in the electronic supplement in section S2.

As described earlier, capillary pressures are present for contact angles $\neq$ 90° and considered in the case of partially filled channels, only. Therefore, the capillary pressure in a channel drops from a finite value to zero when the state changes from partially filled to either full or empty. On the other hand, if the state changes from either full or empty to partially filled, the capillary pressure jumps from zero to a finite value. However, numerical simulations may become unstable in case of discontinuous pressure jumps. Therefore, an interpolation strategy for capillary pressure is necessary at the interconnections of channels, and also at the interconnections to other model blocks. The interpolation of capillary pressure also allows for a continuous transition of the capillary pressure in case of channels with different channel cross-sections or contact angles. Compatibility of the interpolation method with the Simscape programming has been achieved by introducing an additional set of meniscus-tracking signals that are exchanged between connected blocks and scale the capillary pressures at the boundaries. Details are provided in section S3 of the electronic supplement.

Chamber models

VOLUME CONSERVATION As network-simulation is based on Kirchhoffs laws, the through-variable q is conserved. Sources and drains are given by "vent ports" in analogy to "ground" in electrical lumped model networks. In order to allow for the modelling of elements that break volume conservation such as models for gas compression or liquid-vapour generation, these models internally include a source or drain. In contrast to the "vent port" which does not change pressure upon volume flow, these models adjust their pressure according to the appropriate physical state equations such as e.g. the ideal gas law.

VENTED CHAMBER models fulfil a variety of purposes. The simplest case is a vented chamber that can act as a sample or reagent inlet. Thereby, the integrated "vent port" provides the balancing gas flow (source term) to allow liquid to flow out of the chamber. The pressure at the "vent port" always remains at the ambient pressure p_0. Further purposes are the integration of vented mixing or waste chambers into the network model.

In general, the shape of chambers is not a simple geometric form due to the space limitations given by the surrounding microfluidic elements and the requirement to allow for complete emptying of chambers during liquid transfer. Therefore, a relation $h(V_{liquid})$ between the amount of liquid in the chamber, V_{liquid}, and the height of the resulting hydrostatic column in the chamber, h, needs to be established. This function allows then for the calculation of the centrifugal pressure, generated by the liquid in the chamber.
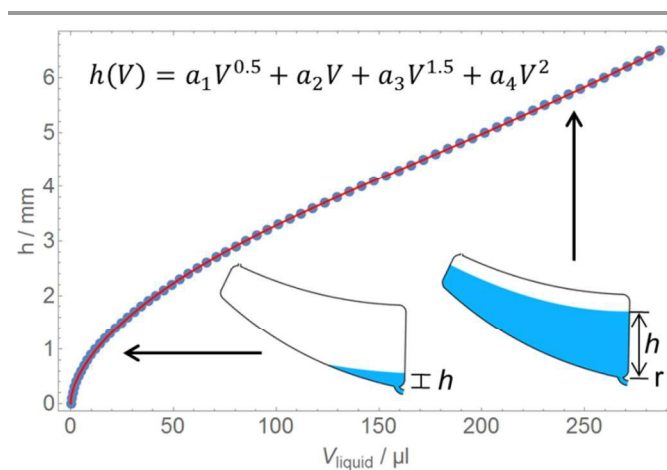

Figure 6: Graph of the fill level $h(V_{liquid})$ fit-function (red line) together with the set of volumes determined from the CAD model of the chamber (blue dots) for the illustrated chamber. The parameters of the fit function are given by a1, a2, a3 and a4.

The $h(V_{liquid})$ function can be determined from the CAD model of the chamber in two steps. The first step is to generate a set of $V_{liquid}(h)$ values for a sufficiently large number of fill-heights h. The second step is to fit this data, using a suitable fit function as shown in Figure 6. Based on the resulting $h(V_{liquid})$ function, the centrifugal pressure inside a chamber can be calculated as stated in Table 2. For all centrifugal microfluidic chamber models, the meniscus in a partially filled chamber is

approximated as an isoradial interface. This approximation neglects cases in which liquid spilling in chambers due to high angular accelerations at low spinning frequencies does have a significant impact on the fluidics.

Table 2: Lists of physical effects considered in chamber models. **r** is the distance between the outlet of a chamber and the centre of rotation. The relative azimuthal position of the outlet on the chamber is **G** with **G = 1** corresponding to the outlet on the right side of a chamber – see Figure 6 – and **G = −1** corresponding to the outlet on the left side. n_{air} is the model internal variable for the amount of air inside a closed chamber. **R** is the universal gas constant and **T** stands for the system temperature. V_{tot} states the volume of a closed chamber. C_1, C_2 and C_3 are constants of the Antoine equation for water vapour pressure calculation, derived by least squares fit of pressure data from Wexler et. al.[37] If material compliance in pressure chambers is considered B_0 corresponds to the chamber volume in absence of pneumatic overpressure and B_1 & B_2 are fit constants describing the volume increase with pneumatic overpressure due to elastic deformation of the chamber walls.

Centrifugal pressure[21]	$$p_{cent} = \frac{\rho}{2}\omega^2\left(r^2 - \left(r - h\left(V_{liquid}(t)\right)\right)^2\right)$$
Euler pressure[21]	$$p_{euler} = -\rho\,L_i\,\frac{d\omega}{dt}\,r\,(G-1)/2, \qquad \frac{d\omega}{dt} > 0$$ $$p_{euler} = \rho\,L_i\frac{d\omega}{dt}\,r\,(G+1)/2, \qquad \frac{d\omega}{dt} \le 0$$
Pneumatic pressure of air[38]	$$p_{\text{pneu\_id}} = (n_{air}\,R\,T)/(V_{tot} - V_{liquid})$$
Pneumatic pressure of vapour[37]	$$p_{vap}(T) = C_1\,e^{\left(C_2\frac{T}{C_3+T}\right)}$$ $C_1 = 610.78\ Pa$, $C_2 = 17.08085$ and $C_3 = 234.175\ K$
Volume change due to material compliance	$$V_{chamber} = B_0 + B_1\Delta p + B_2\Delta p^2$$

In partially filled and filled chambers, Euler forces lead to a pressure increase that depends on the azimuthal position inside the chamber. Therefore, the effect on connected elements depends not only on the angular acceleration, but also on the position G of the connection between chamber and connected channel and the details of the geometry of the chamber. Under typical operation conditions, the Euler pressure in chambers is considerably smaller than the pressures in the connected network. Therefore, the Euler pressure is approximated in analogy to an isoradial channel by a liquid filled isoradial length L_i which generates the Euler pressure if liquid is present in the chamber. The corresponding terms – given in Table 2 – depend on the direction of acceleration and are derived in section S 4 of the electronic supplement.

All other forces, namely inertia, Coriolis, capillary and viscous forces are typically negligibly small in chambers, in particular when compared to the respective values inside connected channels. If required, these forces – with the exception of Coriolis force – can be implemented analogous to the channel

models with the equations listed in Table 1. A more in depth discussion of the reasons why the Coriolis force is neglected in lumped models of centrifugal microfluidic chambers is provided in section S11 of the electronic supplement.

PNEUMATIC CHAMBERS The next types of chambers are unvented, pneumatic chambers. Pneumatic chamber models contain all features of vented chamber models and extend them by keeping track of the pneumatic pressure change during simulation.

Pressure increase is caused by
1.) Liquid entering the chamber and compressing the gas
2.) Liquid entering the chamber and saturating the already present gas with vapour
3.) Increase of the temperature of the present gas
4.) Evaporation of liquid due to temperature increase leading to higher amounts of vapour

Pressure decrease in turn is caused by
1.) Decompression of the gas due to liquid leaving the chamber
2.) Decrease of the gas temperature
3.) Condensation of liquid due to temperature decrease leading to smaller amounts of vapour

In the case that a pneumatic chamber is not in contact with liquid or the temperature remains low, so that the relative influence of vapour pressure is negligible, the liquid vapour pressure can be omitted and the pneumatic pressure of the air is calculated according to the ideal gas law.

Due to the large surface to volume ratios in microfluidics, gases in contact with liquid surfaces quickly saturate with the respective liquid vapour. This can lead to a substantial additional pneumatic pressure e.g. in PCR applications where the saturated vapour pressure can reach up to 850 mbar[39]. The saturated water vapour pressure can be modeled using the Antoine equation[40] and is considered in simulations by adding the pressure of the liquid vapour p_{vap} to the pneumatic pressure of the air. At the beginning of a simulation, the initial amount of air n_{air} is determined to ensure $p_{vap} + p_{air} = p_0$ with the atmospheric pressure p_0. During simulation, the pneumatic pressure in the chamber is calculated to $p_{pneu} = (n_{air}*R*T) / (V_{tot} - V_{liq}) + p_{vap}(T)$.

In the case of pneumatic chambers formed in flexible foil materials, pneumatic chamber models can be enriched with a model for the pressure dependent volume increase of the chamber due to material compliance, see Figure 7 and Table 2. With this model, the pressure dependent chamber-volume $V_{chamber}$ replaces the constant parameter V_{tot} in the calculation of the overpressure inside the pneumatic chamber.

In this paper, we will restrict the discussion of chamber models to vented and pneumatic (unvented) chambers without further features. Nevertheless, we would like to point out that chambers with excess liquid capturing features for liquid metering[41] can easily be realized. Also chambers with more

than two fluidic connections to the surrounding network can be devised, although the number of wetting states such models need to take into account increases dramatically.
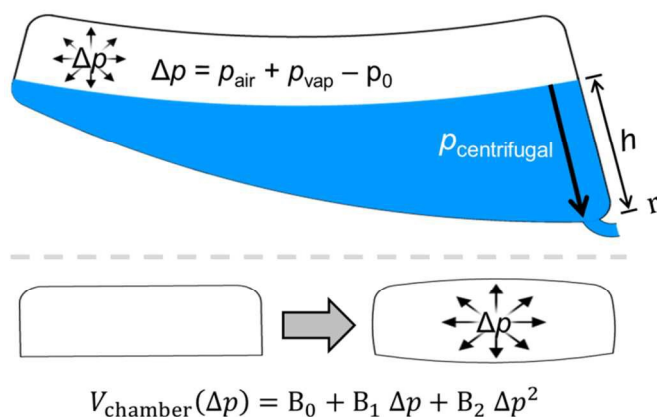

Figure 7: Top: Illustration of a pneumatic chamber. The liquid inside the chamber compresses the present gas. Liquid vapour pressure adds to the total pressure. The overpressure Δp w.r.t.. atmospheric pressure leads to compliance in chambers formed in flexible foil materials. **Bottom:** Illustration of material compliance in pneumatic chambers formed from or sealed with flexible foil materials. The given empirical formula is used to fit the chamber volume dependence on overpressure inside a chamber. The fit parameters are determined empirically dependent on foil material and chamber geometry.

T-junctions

To allow for complex centrifugal microfluidic networks, branching points for channels need to be available. At these T-junctions, a flow division takes place according to Kirchhoff's laws. To allow for correct simulations under two-phase flow conditions, the wetting-state-signals and the capillary pressure interpolation signals are managed by the T-junction models. Details of the implementation and a discussion of the considered forces are provided in section S 4.3 of the electronic supplement.

Capillary valves

Hydrophobic patch valves[42] can simply be represented by a channel model with appropriately chosen dimensions and contact angles. This is also true for geometric valves with contact angles > 90° that rely on an abrupt narrowing of channel dimensions. Geometric valves that rely on an abrupt widening in a channel to generate pinning[11,43] are currently represented by a modified channel model in which the capillary pressure inside a channel is replaced by the burst pressure of the valve. More sophisticated analytical models for the burst pressure of capillary valves considering different geometries can be found in the literature[44]. If desired, the implementation of these analytical models in lumped element models is straight forward and can be realized simply by adding the respective equation as a pressure source to the respective element.

Controller models

Controller models are required if e.g. a specific liquid flow rate inside a channel has to be maintained over a certain period of

time. In this case, the lumped element model for the channel is augmented with the ability to control e.g. the spin protocol of the system during simulation. Thereby, the controller model derives a spin protocol to appropriately compensate the typically complex pressure condition changes during liquid transfer.

To demonstrate this approach, such a controller model is employed in the section "Application case 2 – Flowrate control". Details on the implementation and possible extensions of controller models are provided in the electronic supplement in section S6.

Simulation based layout and robustness analysis

The contribution of network simulation to the development of centrifugal microfluidic lab-on-a-chip systems has two aspects. First, it allows to increase the development speed during the layout phase of a chip because it provides detailed insight into the system dynamics. Due to the typically short time-to-result for network simulations (seconds to minutes), geometry adaptations of channels and chambers as well as changes in temperature or spin protocol can be tested in order to devise a functional layout together with its operation protocols. If the simulation of the concept-layout should show considerable unforeseen flaws due to undesired interactions of microfluidic elements, an alternative concept can be developed rapidly based on the simulation results.

The second aspect is the possibility to analyse the impact of manufacturing tolerances and operation condition variations on the system performance of an established layout. Here the speed and ease of adaptation of network-simulations allow for the consideration of a potentially large number of system parameters. In the following section, Table 3 lists the error sources that were taken into account for this robustness analysis.

Application case 1: Mixing by reciprocation and rotational acceleration triggered compression valving

In this section, we demonstrate the use of system-level network simulations for the prediction of system dynamics and robustness on the example of a fluidic structure introduced in Fig. 2 for mixing of two liquids and subsequent valving.

Design goals

The first design goal of the fluidic structure is to achieve fast and thorough mixing of two liquids by reciprocation. To this end, the Reynolds-number $Re = \rho v d / \eta$ of the flow between *pneumatic chamber 1* and *mixing chamber* needs to be as high as possible. Here ρ denotes the liquid density, v is the liquid velocity, d is given by the shorter length of the rectangular channel between the chambers and η is the dynamic viscosity of the liquid. The second design goal is to robustly prevent valving of the liquids during the mixing steps and to ensure valving after mixing is finished.

OPERATION CONCEPT AND LAYOUT

In Figure 8, the operation concept for the fluidics is illustrated. In step A, two distinct liquids are filled into the *inlet chamber* which is indicated by the colour gradient. By increase of the spin frequency, both liquids are transferred in step B to *pneumatic chamber 1* (main part) and *mixing chamber* (small part). Thereby, the gas in the *pneumatic chambers* is compressed. In steady state, the pneumatic overpressure in the *pneumatic chambers* is equal to the centrifugal pressure of the liquid column between the meniscus in the *mixing chamber* and the meniscus in *pneumatic chamber 1*.

From here on, a difference in radial distance between menisci – as indicated in Figure 8 by *Δh* – will be named hydrostatic height. After reduction of the spin frequency in step C, the pneumatic overpressure exceeds the centrifugal pressure and the liquids are pushed into the inlet channel, the mixing channel and the siphon channel. With a deceleration rate of 20 Hz s^{-1} and a minimal spin frequency of 20 Hz, the increase in hydrostatic height in the inlet channel and the siphon channel compensates the decrease in centrifugal pressure that comes along with the reduction of the spin frequency. Therefore, the *siphon valve* is not triggered. As a result, the liquids are transferred to the *mixing chamber* until the centrifugal pressure, generated by the hydrostatic height between the *mixing chamber* and the *pressure chamber 1,* equals the residual pneumatic overpressure in the *pressure chambers 1 & 2*.

Repeated increase and decrease of the spin frequency with ± 10 Hz s^{-1} between 20 Hz and 40 Hz mixes the two liquids by transporting them back and forth between the *mixing chamber* and *pneumatic chamber 1*. After mixing is complete – step D –, the spin frequency is decreased starting from 40 Hz with a deceleration rate of 30 Hz s^{-1} to 1 Hz.

Inside the *siphon channel*, if the deceleration rate is sufficiently high, the sum of centrifugal pressure, viscous pressure and capillary pressure of the advancing meniscus – which all counteract the filling of the siphon channel – drops below the pneumatic overpressure of the pneumatic chambers. Therefore, the *siphon channel* fills with liquid beyond the critical fill-level of 70% (step E)**.** By increase of the spin frequency to 30 Hz in step F, the liquid is pumped from the *mixing chamber* and *pneumatic chamber 1* to the *downstream fluidics*. Following this operation concept, the *mixing channel* is designed to have the lowest possible fluidic resistance that allows robust valving. If the resistance of the *mixing channel* is too small, the liquid transfer to the *mixing chamber* in step E reduces the pneumatic overpressure in *pneumatic chamber 1* too fast to allow for the priming of the *siphon channel*. If, on the other hand, the resistance of the *mixing channel* is large, priming is ensured, but the maximum of the flow rate during reciprocation mixing is low and with it, the mixing performance[32].

Pneumatic chamber compliance

As explained earlier, pneumatic chambers formed in flexible foil materials show material compliance. Currently, the parameters for the fit functions are derived experimentally after manufacturing, while during chip-development an estimate of the compliance is taken into account. For the given system, the resulting relationship between the total volume of *pneumatic chambers 1 & 2* and the pneumatic overpressure is depicted in Figure 9.
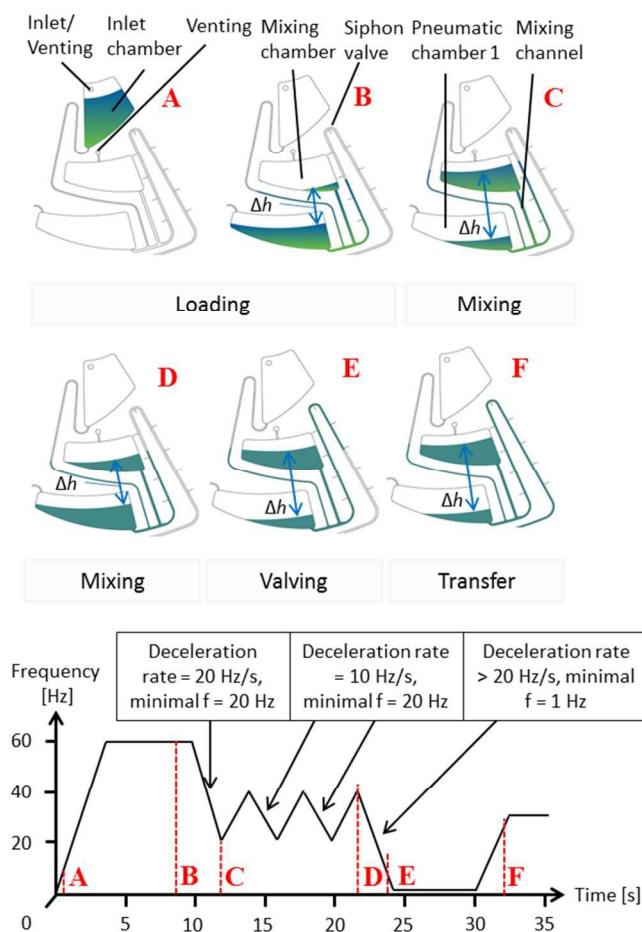

Figure 8: Top: Illustration of the process of mixing by reciprocation and rotational acceleration triggered compression valving. **Bottom:** Spin protocol to operate the fluidics.

Simulation predictions and experimental results

In Figure 9, the simulations are compared to experimental results for the liquid fill-levels in the *mixing chamber*, the *pneumatic chamber 1* and the *siphon channel*. The liquid volumes in the respective chambers were determined by functions that relate the meniscus position to the liquid volume inside the chamber. Thereby, the meniscus position was observed during the experiments by image acquisition and the functions were derived from the CAD models of the chambers analogous to the procedure to derive their inverse – the *h(V)* functions to simulate the centrifugal pressures in chamber models. The images were acquired during processing in a LabDisk Player (QIAGEN Lake Constance, Stockach,

Germany) via a custom built stroboscopic image acquisition system added to the LabDisk Player by Biofluidix GmbH, Germany. It can be seen that experimental results for the liquid volumes in the chambers fit very well to the simulations, thus, the simulation value for the peak flow rate of 40 µl s^{-1} in the mixing channel is assumed to be a good approximation of the true flow rate. To illustrate the pressure dynamics in the system, obtained simulation results for the pressures in the fluidic network are provided in the electronic supplement section S10. We expect the structure to provide very efficient mixing because the Reynolds-number of the flow inside the mixing channel is increased by a factor of 140 when compared to the reciprocation mixing experiments reported by Noroozi et. al[32]. As discussed before, the Coriolis force induced increase of the effective flow resistance of the channels can be neglected in the experiments. Details on the performed 3D-CFD-simulations of the effect with COMSOL Multiphysics® 5.1 (www.comsol.com, 2015) are provided in section S 7 of the electronic supplement.
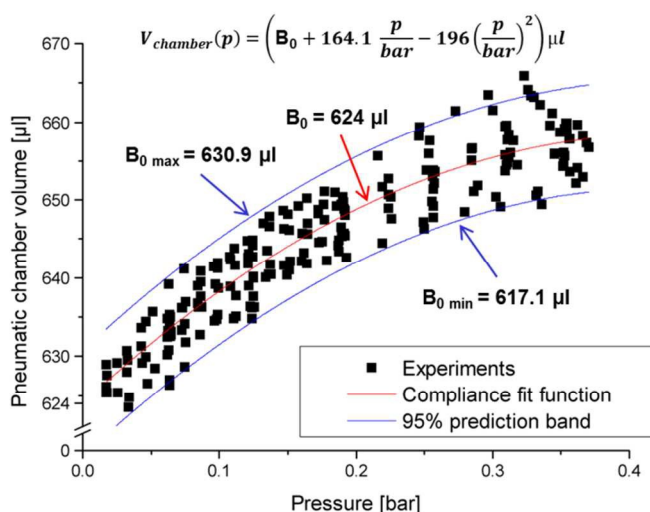
roughness of the substrate material is already considered by the robustness analysis as the values and variations of the advancing and receding contact angle do not only reflect measurement errors and surface energy variations but also the surface roughness of the substrate material. The impact of surface roughness on the fluidic resistance of channels is taken into account by the appropriate choice of the channel diameter and its variations. We performed one simulation series with the nominal values for all parameters, one series with the combination of the individual operation condition variations that favour valving the most, and one series with the combination that hampers valving the most. Each series was performed by consecutively increasing the simulated final deceleration rate until liquid transfer to the *downstream fluidics* was predicted. To demonstrate the significance of compliance for pressure chambers in flexible materials, these simulations were performed in two variants. The first variant considered compliance and the second neglected compliance. The results are listed in Table 4.
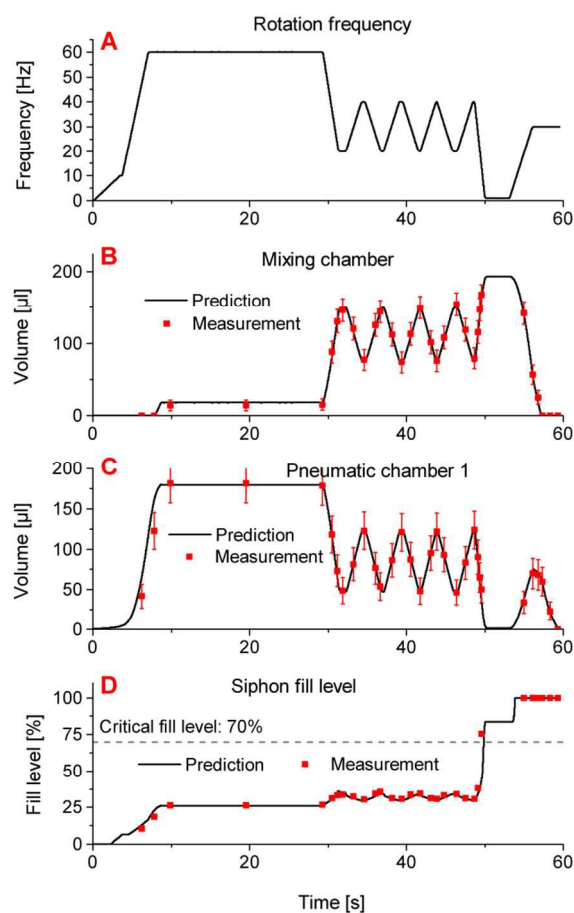

Figure 9: Experimental results for the volume of *pneumatic chambers 1 & 2* as function of the pneumatic overpressure in the chambers. The values of B_0 that correspond to the 95 % prediction band are indicated with $B_{0\ min}$ and $B_{0\ max}$.

Robustness analysis

A critical parameter for reciprocation mixing and subsequent pneumatic valving is the deceleration rate during mixing. On the one hand, deceleration should be as high as possible for strong mixing flows, on the other hand, it must be sufficiently low to avoid premature priming of the siphon. We demonstrate simulation based robustness analysis of this critical deceleration rate taking into account manufacturing tolerances and varying operation conditions. For this purpose, a series of simulations with variations of the channel geometries and temperature conditions were carried out to determine the maximum deceleration rate that can be used during mixing. This maximum deceleration rate is derived by finding the minimum deceleration that triggers the siphon. The chosen variations are listed in Table 3. We would like to point out, that surface

Figure 10: Comparison between simulation prediction and the results of one experiment for the discussed fluidic process. The experiment was performed using 200 µl of DI water. The spin protocol is depicted in **A**. For the simulation, the nominal parameter values as listed in Table 3 were used and the channel and chamber models took all effects into account that are stated in Table 1 and Table 2. In addition, capillary hysteresis was also considered. **B** and **C:** Liquid volumes inside *mixing chamber* and *pneumatic chamber 1* during system operation. The black continuous line corresponds to the simulation prediction based on the spin

protocol in **A**. The red dots indicate experimental results. The error bars correspond to the measurement accuracy of the fill levels in the respective chambers and the expected volume error based on manufacturing tolerances of the chambers. **D:** Siphon fill levels as indicated in Figure 3 and Figure 8. The error bars correspond to the measurement error of the meniscus position and lie within the measurement points. If the liquid fill level exceeds the critical fill level, the liquid is transferred to the downstream fluidics during the final increase of spin frequency between 54 s and 60 s.

Table 3: Parameters for operation condition variations. The simulations for robustness analysis use either the combination of parameters that favour or hamper siphon priming. For siphon and mixing channel dimensions, the tolerance is given by the manufacturing tolerances of the milling process. The tolerance of the pipetted volume is taken from the pipette manufacturer specifications. The temperature measurement error together with the variations during one experiment are estimated to be of or below 2°C. The advancing and receding contact angles between COC and water were measured using a sessile drop measurement setup. The used contact angle variations correspond to the standard deviation of the measurements multiplied by two. (95% confidence interval). The variation of the compliance function parameter B_0 was determined together with the compliance fit function. See Figure 9.

Varied parameters	Nominal value	Valving favoured	Valving hampered
Siphon channel dimensions (w x d)	287 µm x 291 µm	+ 5 µm / + 5 µm	- 5 µm / - 5 µm
Mixing channel dimensions (w/d)	391 µm x 396 µm	- 5 µm	+ 5 µm
Pipetted volume	200 µl	+ 2 µl	- 2 µl
Temperature	23 °C	- 2 °C	+ 2 °C
Advancing / receding contact angle	98.8 ° / 74.4 °	-8.9° / + 4.3°	+ 8.9° / - 4.3°
Compliance function parameter B_0	624 µl	-6.9 µl	+ 6.9 µl

Table 4: Simulation predictions for the minimal/critical deceleration rate, needed to trigger the siphon valve. The results are obtained by considering the three parameter sets listed in Table 3. The influence of material compliance on the minimal deceleration rate that ensures valving is studied by comparing simulations that take compliance into account to simulations that do not consider flexibility of the chip material.

	Critical deceleration [Hz s⁻¹] compliance considered	Critical deceleration [Hz s⁻¹] compliance **not** considered
Valving favoured	15.5	20.5
Valving nominal	22.5	29
Valving hampered	30.5	39.5

To compare the predicted robustness-corridor with the experiment, the same procedure as in the simulation was also used in 8 experiments. 200 µl of water were filled into the *inlet chamber* and transferred to *pneumatic chamber 1* by centrifugation at 40 Hz. Next, the system was decelerated with

an initial deceleration rate of 12 Hz s⁻¹ which is insufficient for priming the siphon. After re-acceleration to 40 Hz, the deceleration step was repeated with a deceleration rate increased by 0.5 Hz s⁻¹. This procedure was continued until the siphon valve was triggered. The experimental result for the minimal needed deceleration rate in 8 experiments is 19.6 Hz s⁻¹ ± 0.9 Hz s⁻¹. The minimal and maximal priming deceleration rates were 19 Hz s⁻¹ and 21 Hz s⁻¹, respectively. These results are in good agreement with the predictions considering pneumatic chamber compliance.

Liquid property influence on pumping and valving

In order to demonstrate the applicability of network-simulation for the prediction of lab-on-a-chip system behaviour, three additional liquids relevant for biochemical analysis were used for the process of mixing and subsequent valving. The liquids were selected in order to represent different fluidic challenges, namely low contact angle (50% ethanol in water w/w), high viscosity (50% glycerine in water w/w) and large contact angle hysteresis (blood plasma). Because blood plasma contains a high concentration of proteins that coat microfluidic channel walls manufactured in cyclic-olefin-copolymer (COC) it changes the contact angle between plasma and channel wall upon contact[45]. The advancing contact angle between plasma and COC was measured to 92.0° ± 2.4°. After contact, the advancing contact angle changes to 45.9° ± 2.3° due to the coating. In order to take this behaviour into account, the lumped models for channels were enriched with the option to register coated channel segments during operation and choose the appropriate advancing contact angle. The implementation of this option is described in the electronic supplement in section S 2.

Table 5: Table of measured properties of test liquids at 22°C. The viscosities were measured with an Anton Paar Physica MCR 101 rheometer. Contact angles and surface tensions were determined on a DataPhysics OCA 15 Plus device.

	Ethanol (50%)	Glycerol (50%)	Blood plasma
Advancing contact angle before contact [°]	52.5 ± 2.4	88 ± 1.2	92.0 ± 2.3
Advancing contact angle after contact [°]	52.5 ± 2.4	88 ± 1.2	45.9 ± 2.3
Receding contact angle [°]	30 ± 4.4	79 ± 4.3	0
Viscosity [mPas]	2.56 ± 0.02	5.62 ± 0.02	1.88 ± 0.11
Surface tension [mN/m]	30.7 ± 3.2	58.7 ± 2.5	60.7 ± 1.5

Simulation and validation procedure

In order to derive a suitable frequency protocol for the mixing and subsequent valving operation, the liquid properties in the established simulation model were adjusted to the values

specified in Table 5. All other parameters such as channel dimensions, liquid volume, temperature or compliance function parameter B_0 were set to the nominal values. In the case of blood plasma, the additional feature for tracking of coated channel walls was activated. As for water (Figure 10) the simulation predictions and experimental results for the volumes in the *mixing chamber* and *pneumatic chamber 1* as well as the fill level in the *siphon channel* are in excellent agreement for all liquids. The corresponding graphs are shown and discussed in the electronic supplement in section S8.

Application case 2: Flow rate control

For the second application case, a network simulation model is developed that derives a spin protocol to maintain pre-defined flowrates within centrifugal microfluidic networks. This can be used to control shear rates in the liquids involved or to yield defined contact times between liquid and potentially functionalized surfaces in channels and chambers. Here, the configuration depicted in Figure 3 and Figure 8 is considered again. The model is applied to provide a constant flow of 3.5 µl s^{-1} in the *mixing channel* during transfer between *pneumatic chamber 1* and the *mixing chamber* and vice versa. Thereby, the derived spin protocol must compensate the continuous change of the hydrostatic pressure and pneumatic pressure during the transfer. For the pneumatic pressure, material compliance is taken into account.

The model block for the *mixing channel* was extended by a controller. The spin frequency *f* of the system during simulation is adjusted according to

$$\dot{f} = A(q_t - q(t)) \ (5)$$

Here, q_t denotes the target flow rate (3.5µl s^{-1} in this example) and $q(t)$ stands for the flow rate inside the *mixing channel*. A is the gain factor of the proportional controller ($10^4 \ s^{-1}\mu l^{-1}$) in this example). The advantages of the high gain factor of 10^4 in the controller are explained in the electronic supplementary, section S6. To ensure a realistic spin protocol as a result of the simulation, conditional programming limits the maximal acceleration/deceleration rate to 30 Hz s^{-1} if the calculated $\dot{f}$ would otherwise exceed the capabilities of the experimental setup.

The fluidics of application case 2 is as follows: A volume of 140 µl liquid is filled into the *inlet chamber* and transferred to *pneumatic chamber 1* by spinning at 57 Hz. This frequency has been calculated in order to have a filled mixing channel and an empty mixing chamber as starting condition. The next step is the transfer of the liquid from *pneumatic chamber 1* to the *mixing chamber* with a flow rate of 3.5 µl s^{-1}. When all liquid is transferred to the *mixing chamber,* the flow is reversed and all liquid is transferred back to *pneumatic chamber 1,* again with a flow rate of 3.5 µl s^{-1}.

In Figure 11 A, a typical spin protocol available without simulation – interpolating linearly between the 57 Hz and 0 Hz over 40 s – and the spin protocol derived by simulation using the controller module is depicted. Figure 11 B shows the

experimental results and a 4th order polynomial fit for the liquid volumes inside the mixing chamber as a function of time, if the controller model based frequency protocol is used.

In Figure 11 C, the experimentally determined liquid volumes in the mixing chamber resulting from the simple linear frequency protocol and the corresponding 4th order polynomial fit are shown.

In Figure 11 D, the flow rates in the channel between mixing chamber and pneumatic chamber 1 are depicted. They were derived by differentiation of 4th order polynomial fit functions from B and C and show that the simulation based spin protocol leads to significantly superior flow-rate stability when compared to the linear interpolation spin protocol.
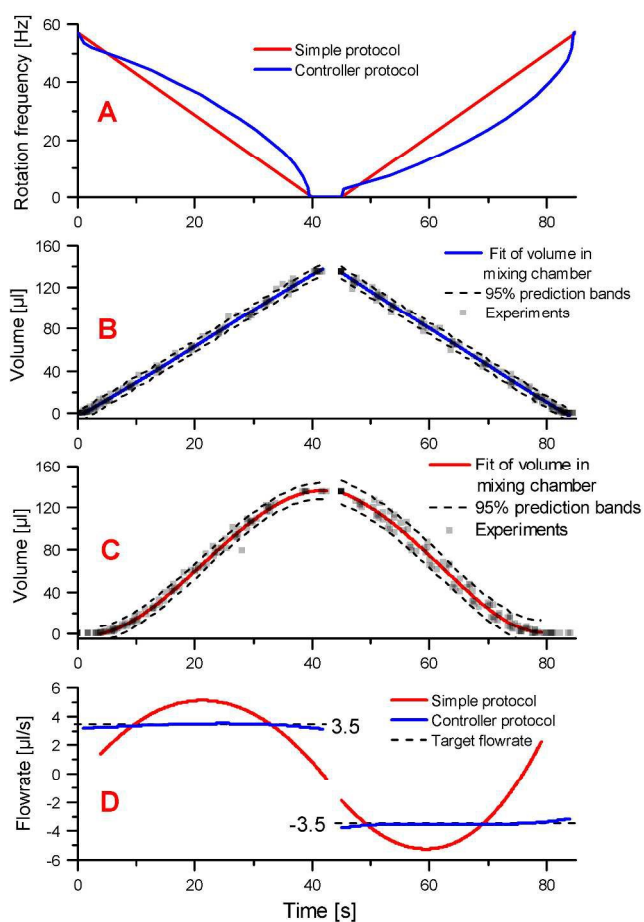

Figure 11: A: Linear and simulation derived spin protocols for the transfer of water from the pneumatic chamber to the mixing chamber and vice versa with a constant target flowrate of 3.5 µl s^{-1}. **B:** Experimental results using the simulation based spin protocol. The grey dots represent measurements of the liquid volume in the mixing chamber from 8 individual experiments. The experimental data was fitted with two separate 4th order polynomials. In the graph, the prediction bands for 95% of the experimental measurements are depicted. **C:** Same information as B for the case of the simplified linear spin protocol. **D:** Based on the fit-functions, the flowrates resulting from the two spin protocols are calculated by differentiation.

During the first pump step, the flow rate is (3.38 ± 0.10) µl s^{-1} with a maximum / minimum flow rate of 3.51 µl s^{-1} and 3.12 µl s^{-1}, respectively. During the second pump step, the flow rate is (3.51 ± 0.11) µl s^{-1} with a maximum / minimum flow rate of

3.79 µl s^{-1} and 3.17 µl s^{-1} respectively. The simple frequency protocol yields a flow rate of (3.53 ± 1.46) µl s^{-1} during the first pump step with a minimum of 0 µl s^{-1} and a maximum of 5.25 µl s^{-1}. During the second pump step the flow rate is (3.35 ± 1.92) µl s^{-1} with a maximum of 5.25 µl s^{-1} and a minimum of 0 µl s^{-1}.

Conclusions

We introduced advanced lumped models for network-simulation in centrifugal microfluidics and demonstrated their benefit for centrifugal microfluidic lab-on-a-chip layout, including robustness analysis of the unit operations liquid transport, valving, and mixing. Using the network-simulation approach, complex and dynamic interactions can be simulated both fast and with high precision. The short time to result allows to test several fluidic layout concepts and optimize the most promising one – in-silico – before the first prototype is manufactured. The simulations consider two phase flow with varying liquid properties such as viscosity and surface tension. Manufacturing tolerances can be taken into account as well as material compliance. Last but not least, we showed that controller concepts can be used during simulation to derive optimal spin protocols to follow a pre-defined flow-rate profile despite complex pressure condition variations. Such controllers can be used to provide any desired flow-rate protocol in channels and chambers. We expect that the impact of the network-simulation approach on the centrifugal microfluidic lab-on-a-chip community will increase proportionally to the degree of chip-integration, the number of available unit operations, the availability of advanced lumped models and the need for robustness assessments of chips during their development for the market.

Outlook

One future route to extend the impact of network simulation in centrifugal microfluidics is the introduction of lumped models that consider multiple liquid phases – such as for example oil and water for the layout of droplet microfluidic systems.

Another route is the consideration of multi-species transport and chemical reactions in bulk as well as on functionalized surfaces. Such simulations could be used to derive optimized flow rate protocols to minimize reaction times for (bio) chemical reactions with transport limited reaction kinetics.

Acknowledgements

Notes and references
^{a} Hahn-Schickard – Institut für Mikro- und Informationstechnik, Georges-Koehler-Allee 103, 79110 Freiburg, Germany.
Email: Ingmar.Schwarz@Hahn-Schickard.de

^{b} Laboratory for MEMS Applications, IMTEK - Department of Microsystems Engineering, University of Freiburg, Georges-Koehler-Allee 103, 79110 Freiburg, Germany

^{c} BIOSS – Centre for Biological Signalling Studies, University of Freiburg, 79110 Freiburg, Germany

References

1 O. Strohmeier et al., *Chem. Soc. Rev.*, 2015, **44**, 6187–6229.
2 E. Roy et al., *Lab Chip*, 2015, **15**, 406–416.
3 R. Gorkin et al., *Lab Chip*, 2010, **10**, 1758–1773.
4 a) J. Ducrée et al., *J. Micromech. Microeng.*, 2007, **17**, 103–115; b) S. Lai et al., *Analytical chemistry*, 2004, **76**, 1832–1837; c) D. C. Duffy et al., *Anal. Chem.*, 1999, **71**, 4669–4678;
5 J. Siegrist et al., *Microfluid Nanofluid*, 2010, **9**, 55–63.
6 a) J.-M. Park et al., *Lab Chip*, 2007, **7**, 557–564; b) K. Abi-Samra et al., *Lab Chip*, 2011, **11**, 723–726;
7 J. L. Garcia-Cordero et al., *Lab Chip*, 2010, **10**, 2680–2687.
8 Thio, Tzer Hwai Gilbert et al., *Lab Chip*, 2013, **13**, 3199–3209.
9 M. M. Aeinehvand et al., *Lab Chip*, 2015, **15**, 3358–3369.
10 J. Steigert et al., *Lab Chip*, 2006, **6**, 1040–1044.
11 H. Cho et al., *J. Colloid. Interface. Sci.*, 2007, **306**, 379–385.
12 C. T. Schembri et al., *J. Autom. Chem.*, 1995, **3**, 99–104.
13 R. Gorkin III et al., *Lab Chip*, 2012, **12**, 2894–2902.
14 a) D. J. Kinahan et al., *RSC Adv*, 2015, **5**, 1818–1826; b) D. J. Kinahan et al., *Lab Chip*, 2014, **14**, 2249–2258;
15 W. Al-Faqheri et al., *PloS one*, 2013, **8**, e58523.
16 a) F. Schwemmer et al., *Lab Chip*, 2015, **15**, 1545–1553; b) S. Zehnle et al., in *MicroTAS 2012*, Curran, 2014, vol. 2, pp. 869–871;
17 S. Zehnle et al., *Microfluid Nanofluid*, 2015, **19**, 1259–1269.
18 R. Gorkin III et al., *Microfluid Nanofluid*, 2010, **9**, 541–549.
19 N. Godino et al., *Lab Chip*, 2013, **13**, 685–694.
20 K. Abi-Samra et al., *Microfluid Nanofluid*, 2011, **11**, 643–652.
21 S. Zehnle et al., *Lab Chip*, 2012, **12**, 5142–5145.
22 S. Soroori et al., *Microfluid Nanofluid*, 2014, **16**, 1117–1129.
23 M. Wörner, *Microfluid Nanofluid*, 2012, **12**, 841–886.
24 T. Glatzel et al., *Computers & Fluids*, 2008, **37**, 218–235.
25 H. M. Schaedel, *Fluidische Bauelemente und Netzwerke*, Vieweg, Braunschweig, Wiesbaden, 1979.
26 K. W. Oh et al., *Lab Chip*, 2012, **12**, 515–545.
27 M. Schindler and A. Ajdari, *Phys. Rev. Lett.*, 2008, **100**, 44501.
28 F. Jousse et al., *Lab Chip*, 2005, **5**, 646–656.
29 a) N. Gleichmann et al., *Chemical Engineering Journal*, 2008, **135**, S210-S218; b) N. Gleichmann et al., *Microfluid Nanofluid*, 2015, **18**, 1095–1105;
30 a) P. Koltay et al., in *MSM 2002 Int. Conf. on Modeling and Simulation of Microsystems*, pp. 112–115; b) P. Koltay et al., in *MSM 2002 Int. Conf. on Modeling and Simulation of Microsystems*, pp. 170–173;
31 M. Sesterhenn et al., in *MSM 1999 Int. Conf. on Modeling and Simulation of Microsystems*, pp. 538–541.
32 Z. Noroozi et al., *Rev Sci Instrum*, 2009, **80**, 75102.
33 H. Bruus, *Theoretical microfluidics*, Oxford University Press, Oxford, 2008, vol. 18.
34 M. Bahrami, M. M. Yovanovich and J. R. Culham, *Transactions of the ASME*, 2006, **128**, 1036–1044.

Lab on a Chip Accepted Manuscript

35 a) Y. Ukita and Y. Takamura, *Microfluid Nanofluid*, 2013, **15**, 829–837; b) S. Haeberle et al., *Chem. Eng. Technol.*, 2005, **28**, 613–616;

36 a) D. Chakraborty, M. Madou and S. Chakraborty, *Lab Chip*, 2011, **11**, 2823–2826; b) J. Ducrée et al., *Microfluid Nanofluid*, 2006, **2**, 97–105; c) J. Ducrée et al., *Microfluid Nanofluid*, 2006, **2**, 78–84;

37 A. Wexler, *J. Res. Natl. Bur. Stan. Sect. A.*, 1976, **80A**, 775–785.

38 L. D. Landau and E. M. Lifshitz, *Statistical Physics. Volume 5*, Elsevier Science, Burlington, 3rd edn., 1996, v. 5, 9.

39 G. Czilwik et al., *Lab Chip*, 2015, **15**, 1084–1091.

40 G. W. Thomson, *Chem. Rev.*, 1946, **38**, 1–39.

41 F. Schwemmer et al., *Lab Chip*, 2015, **15**, 3250–3258.

42 L. Riegger et al., *J. Micromech. Microeng.*, 2010, **20**, 45021.

43 M. J. Madou et al., *Biomedical Microdevices*, 2001, **3**, 245–254.

44 A. Kazemzadeh et al., *PloS one*, 2013, **8**, e73002.

45 Q. Wei et al., *Angew. Chem. (Int. Ed. in English)*, 2014, **53**, 8004–8031.